Chapter 7
Phosphorous-Based Titania Nanoparticles for the Photocatalytic Abatement of VOCs

Melodj Dosa, Marco Piumetti, Samir Bensaid, and Nunzio Russo

7.1 Introduction

A compound can be classified as Volatile Organic Compound (VOC) when it has a vapor pressure greater than 0.01 kPa at 20 °C [1]. The VOCs can evaporate at room temperature and they are carbon-based substances [2–4]. There are several compounds that are classified as VOCs, with specific physico-chemical and thermodynamics properties [5]. Alkanes, alcohols, halogenated hydrocarbons, aldehydes, ketones, aromatics, paraffins, olefins, and sulfur-based compounds are proper examples of VOCs [6–10].

As is known, VOCs are listed as the major contributors to air pollution. They are toxic substances for both environmental and human health. In the specific, they are responsible of the stratospheric ozone depletion and precursors of ground level smog [11–16].

The VOCs can be emitted by outdoor and indoor sources. Outdoor sources include those produced from industries (chemical and textile) and automotive field. On the other hand, household supplies (paints) and construction materials can be classified as indoor emission sources [10, 17–20].

In order to reduce the VOCs emissions, several technologies were proposed [21–23]. They can be divided into two groups: recovery or destruction. In the former group can be listed absorption, adsorption, biofiltration, condensation or separation by membrane. On the other hand, destruction technologies are characterized by processes able to convert VOCs [5].

Among the latter techniques, the most promising is the photocatalytic decomposition, namely the process in which a pollutant can be decomposed by a photocatalytic material (photocatalyst) in the presence of a light source [24–27].

M. Dosa · M. Piumetti (✉) · S. Bensaid · N. Russo
Department of Applied Science and Technology, Politecnico di Torino, Turin, Italy
e-mail: marco.piumetti@polito.it

M. Piumetti, S. Bensaid (eds.), *Nanostructured Catalysts for Environmental Applications*, https://doi.org/10.1007/978-3-030-58934-9_7

However, the photocatalytic phenomenon is characterized by a complex reaction route. The following parameters are the most important during the photocatalytic reaction: (1) photon absorption, (2) charge transport and trapping, (3) charge transfer, (4) molecular absorption, (5) reaction mechanism, (6) poisons and promoters, (7) surface and material structure [28].

1. **Photon absorption.** This phase is considered as a subsurface step. However, there are two major reasons that can influence what happen on the photocatalyst surface. If in the bulk there are lattice modification (i.e., truncations), on the surface, there are unsaturation that can create different mechanisms of charge transfer and, consequently, diverse process of photon absorption. As a second reason, the surface proton absorption can be influenced by the particles' dimensions: the lower nominal particles radius, the higher surface exposed, the higher optical absorption capacity.
2. **Charge transport and trapping.** The charge originated from the absorption in the photocatalyst subsurface region must reach the surface and be stabilized. Thus, the recombination phenomena with the electron/hole pair must be avoided. This is possible only if the photocatalyst structure is optimized (no recombination phenomena and easy charge transfer from the subsurface to the surface).
3. **Charge transfer.** This step is the core of the photocatalytic reaction. It is an interfacial charge exchange between the photocatalyst and the physi- or chemisorbed molecule. In the specific, the photocatalyst is the donor while the molecule on the surface is the acceptor. The charge transfer can be activated only by a light source. In general, a photocatalyst needs energy to promote its electron from the valence band (VB) to the conduction band (CB). During this electron promotion, holes are originated in the valence band. In these holes, OH groups or water molecules can react and originate $OH^\bullet$ radicals able to oxidize molecules in heterogeneous photocatalysis [29]. This mechanism can be activated by wavelength lower than 380 nm and this is a limitation in the possible utilization of UV-Visible light from the sun.
4. **Molecular absorption.** The photocatalytic phenomenon is influenced by the absorption state of the molecule. This aspect can influence both redox properties and electronic structure of the substance absorbate. Thus, as the molecule is absorbed on the surface, it can be more or less easily converted depending on how it is bonded with the photocatalyst surface.
5. **Reaction mechanism.** This step is complex, and it depends on the aspects analyzed into previous points.
6. **Promoters and poisons.** There are elements that can influence positively or negatively the photocatalytic phenomenon. In the specific, they can modify the reaction mechanism, block the sites, or change the energy (i.e., modification on the band gap energy). For example, the promoters can change the photoabsorption mechanism and they can also boost the charge transfer and the trapping phenomenon. Among the promoter there are platinum, silver, gold, palladium, copper, and rhodium. On the other hand, some elements create surface modifications (in terms of physico-chemical properties) that decrease the

reactivity during the photocatalytic reaction. In the latter case, they are considered as poisons.

7. **Surface and material structure.** The surface properties and structure of the photocatalyst can influence the photocatalytic phenomenon. The optimization of the synthesis procedure of the photocatalyst can arises the physico-chemical and electronic properties of the material. Therefore, the photocatalytic reaction is better performed.

A well-known photocatalyst used for the decomposition of VOCs under UV light is TiO_2. In the photocatalytic reaction, the electrons in the TiO_2 structure are promoted to the anatase conduction band (CB) and the corresponding holes are created in the valence band (VB). During this phenomenon, the $^{\bullet}OH$ and $^{\bullet}O^{2-}$ species are produced, according to the following Eqs. (7.1)–(7.4) [23]:

$$TiO_2 + h\nu \rightarrow h^+(VB) + e^-(CB) \tag{7.1}$$

$$H_2O + h^+(VB) \rightarrow OH^- + H^+ \tag{7.2}$$

$$h^+(VB) + OH^- \rightarrow \bullet OH \tag{7.3}$$

$$O_2 + e^-(CB) \rightarrow \bullet O^{2-} \tag{7.4}$$

These radical species additionally react with VOC molecules.

In this work, we considered ethylene as a model molecule of VOCs. In the specific, the ethylene is decomposed following Eqs. (7.5–7.8) to produce CO_2 and water vapor:

$$\bullet OH + C_2H_4 \rightarrow (C_2H_4)* \tag{7.5}$$

$$(C_2H_4OH)* + \bullet O_2 \rightarrow CO_2 + H_2O \tag{7.6}$$

$$Ti(IV) + e^- \rightarrow Ti(III) \tag{7.7}$$

$$Ti(III) + O_2 \rightarrow Ti(IV) + O^{2-} \tag{7.8}$$

During the last decades, it has been considered the possibility to introduce elements into the TiO_2 framework to improve whole activity with a special focus on the band gap energy. In fact, it has been observed that the presence of some elements, such as phosphorus, zirconium, nitrogen or iron [30–33], may render the TiO_2 active in the visible region.

In the present work, a set of doped TiO_2 systems, having different P-contents (0.6, 0.7, and 3 at.%), was studied. The samples were herein labeled as TiO_2-$P_{0.6}$, TiO_2-$P_{0.7}$, and TiO_2-P_3. For comparison purposes, a pure titania sample, labeled as "TiO_2" was synthesized.

The physico-chemical properties of the samples were investigated by complementary technique, such as X-ray Diffraction (XRD), N_2 physisorption at −196 °C, Field Emission Scanning Electron Microscopy (FESEM), Energy Dispersive X-ray (EDX) analysis, X-ray Photoelectron Spectroscopy (XPS), and (DR)UV-Vis spectroscopy. Then, the catalysts were tested for the total oxidation of ethylene under two different light sources (UVB and UVA radiations).

7.2 Experimental Part

7.2.1 Catalysts Preparation

7.2.1.1 Pure TiO_2

The titania-based catalysts were prepared using the sol-gel method [34, 35] as resumed in Fig. 7.1. Briefly, the pure titania sample, TiO_2, was prepared as follows:

Sixty milliliters of acetic acid (20 vol%, Sigma-Aldrich) was dropwised into 10 g of titanium (IV) butoxide. They were stirred together at room temperature for 4 h. Meanwhile, 6 g of Pluronic 123 (Sigma-Aldrich) was soften into 40 mL of ethanol (Sigma-Aldrich). Then, they were stirred at room temperature for 4 h.

After that, the solution containing Pluronic and ethanol was added to the first one (acetic acid and titanium butoxide) and stirred at room temperature for 24 h.

The obtained gel was placed in a Teflon autoclave and then heated in oven for 48 h at 85 °C. The solid was separated and dried at 80 °C. Finally, the dried powder was calcined at 450 °C for 4 h (heating rate of 1.8 °C min^{-1}).

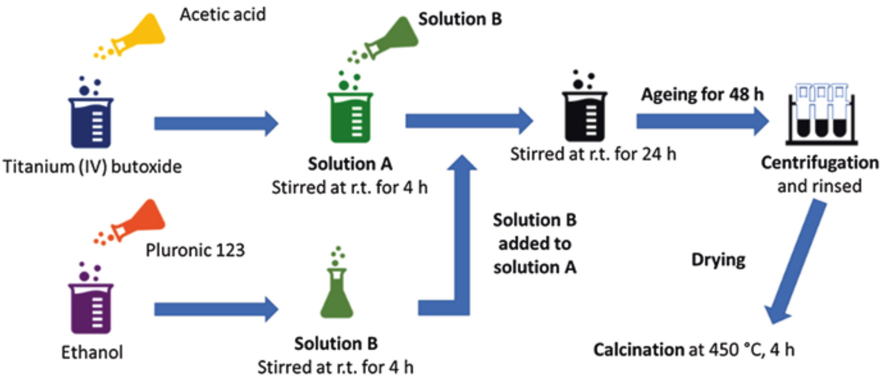

Fig. 7.1 Scheme of the TiO_2 synthesis procedure

7.2.1.2 Phosphorous-Doped TiO_2

Three phosphorous-doped titania samples were synthesized using the procedure described above (Sect. 7.2.1.1) slightly modified. In fact, during the preparation of the solution with acetic acid and titanium butoxide, different amounts of H_3PO_4 (85 wt%, Sigma-Aldrich) were added in order to have the total phosphorus content about 0.6, 0.7, and 3 at.%. The samples were labeled as TiO_2-$P_{0.6}$, TiO_2-$P_{0.7}$, and TiO_2-P_3.

7.2.2 *Catalysts Characterization Techniques*

The powder X-ray diffraction patterns were collected on an X'Pert Philips PW3040 diffractometer using Cu Ka radiation (2θ range = 10–70, step = 0.01θ, time per step = 0.2 s). The diffraction peaks were indexed according to the Powder Data File database (PDF-21999, International Centre of Diffraction Data). The crystallite size was calculated by Scherrer's equation (7.9):

$$D_c = \frac{K\lambda}{\beta \cos\theta} \tag{7.9}$$

where K is a constant (= 0.9), λ is the Cu Kα radiation (= 1.5405 Å), β is the full width at half maximum (FWHM) of the diffraction peak, and θ is the position of the peak.

The N_2 physisorption at −196 °C, performed using a Micromeritics Tristar II 3020 (v1.03, Micromeritics Instrument Corp.), was used to evaluate the total pore volume (V_p), the pore diameter (D_p), and the specific surface area (S_{BET}, calculated using the Brunauer–Emmett–Teller method) on samples previously outgassed at 200 °C for 4 h. The pore volume and pore diameter were estimated by the Barrett-Joyner Halenda (BJH) method, during the desorption phase.

The morphology of the samples was investigated using a field emission scanning electron microscopy (FESEM Zeiss MERLIN, Gemini-II column). Elemental analysis was carried out via energy dispersive X-ray (EDX) analysis (AZTec, Oxford Instruments).

The surface composition of the samples was analyzed via X-ray photoelectron spectroscopy (XPS), performed in a PHI Versa probe apparatus using a band-pass energy of 187.85 eV, a 45° take-off angle, and 100 μm diameter X-ray spot size.

The powder samples were analyzed via the (DR)UV-Vis spectroscopy. A UV-Vis double beam spectrophotometer (Varian Cary 500, Varian) was used. The spectra were collected in 200–450 nm regions, with a resolution of 2 nm.

7.2.3 Photocatalytic Tests

About 0.5 g of catalyst powder was well-spread inside a Pyrex reactor. The reactor was connected to mass flow controllers (Bronkhorst) that continuously feed, during the reaction, a mixture of 500 ppmv of ethylene and 10 vol.% of O_2 (volume balanced with N_2). The outflow from the reactor was analyzed using a nondispersive infrared analyzer (NDIR, Hartmann-Braun) and a gas chromatograph (GC, Varian CP-3800, ShinCarbon ST column, FID). The light sources used have two different wavelengths:

- UVB: wavelength = 312 nm, intensity = 12 W m^{-2}, 230 V, 50 Hz, 0.17 A MONTEPAONE SRL.
- UVA: wavelength = 365 nm, intensity = 8 W m^{-2}, 230 V, 50 Hz, 0.17 A MONTEPAONE SRL.

For each test, the corresponding lamp was located on the top of the reactor. A dark phase was performed before the test, in order to saturate the solid. The lamp was switched on when the system reached a steady-state condition (stable GC peak intensity), and the test ran for a time-on-stream (TOS) of 160 min.

7.3 Results and Discussion

7.3.1 N_2 Physisorption at −196 °C and XRD

Table 7.1 summarizes the textural properties as derived from the N_2 physisorption at −196 °C. All the synthesized samples were compared to P-25 (by Degussa), a commercial titania.

Noteworthy, all the synthesized samples exhibit a higher surface area compared to the commercial sample (P-25). Moreover, the doped samples show higher surface areas (TiO_2-$P_{0.6}$ = 144 $m^2\ g^{-1}$; TiO_2-$P_{0.7}$ = 119 $m^2\ g^{-1}$; TiO_2-P_3 = 168 $m^2\ g^{-1}$) and pore volume (TiO_2-$P_{0.6}$ = 0.50 $cm^3\ g^{-1}$; TiO_2-$P_{0.7}$ = 0.29 $cm^3\ g^{-1}$; TiO_2-P_3 = 0.58 $cm^3\ g^{-1}$) than the pure TiO_2 (S_{BET} = 91 $m^2\ g^{-1}$; V_p = 0.21 $cm^3\ g^{-1}$). This suggests that the

Table 7.1 Results as derived from the N_2 physisorption at −196 °C and XRD analysis

Samples	$S_{BET}{}^{a}$ ($m^2\ g^{-1}$)	$V_p{}^{b}$ ($cm^3\ g^{-1}$)	$D_p{}^{b}$ (nm)	$D_c{}^{c}$ (nm)
P-25	50	0.19	13	30
TiO_2	91	0.21	7	12
TiO_2-$P_{0.6}$	144	0.50	11	11
TiO_2-$P_{0.7}$	119	0.29	7	10
TiO_2-P_3	168	0.58	12	8

[a] Specific surface area calculated by the BET method

[b] Pore volume and pore diameter estimated by the BJH method, during the desorption phase

[c] Crystallite size calculated by the Scherrer's equation

incorporation of P into the TiO_2 framework promotes the textural and structural properties. The crystallite sizes of the samples follow the increasing order:

$$TiO_2 - P_3 \left(= 8\,\text{nm}\right) < TiO_2 - P_{0.7} < TiO_2 - P_{0.6} \left(= 11\,\text{nm}\right).$$

Then, it appears that particles with smaller D_c have more surface defects (i.e., edges and corners) compared to those with higher D_c values [36]. By a theoretical point of view, this effect can be explained considering the volume and area for a single particle. The volume can be expressed by the following equation (Eq. 7.10):

$$V = \frac{4}{3}\pi r^3 \tag{7.10}$$

On the other hand, the particle area can be expressed as follows (Eq. 7.11):

$$A = 4\pi r^2 \tag{7.11}$$

Then, the *A*-to-*V* ratio can be expressed by the following equation (Eq. 7.12):

$$\frac{A}{V} = \frac{3}{r} \tag{7.12}$$

Thus, if the particle radius decreases, the exposed surface area of the particles is higher and, therefore, higher probability to have surface defects for a proper amount (weight) of catalyst.

Since for smaller particles, there is a higher possibility to have more surface defects, there are more unsaturation that are able to create affinity between catalyst surface and the probe molecule (ethylene) [37].

Figure 7.2 shows the XRD diffractograms of the synthesized samples along with P-25 (by Degussa). All the prepared samples provide evidence of the anatase phase. In fact, the transition phase from anatase to rutile typically occurs at temperature above 500 °C [38]. On the other hand, the P-25 also exhibits the presence of rutile phase. The estimated ratio between the two TiO_2 phases for the latter sample is 70/30 (anatase/rutile) [39]. According to the literature, the anatase phase is photocatalytically more reactive than the rutile one due to the electron migration phenomenon that is faster compared to the same occurring in the rutile phase. In addition, the anatase has better photocatalytic activity due to its Fermi level that is higher by about 0.1 eV comparing with that of rutile [40]. Thanks to this better quality, the electron-hole recombination rate is very low [41].

In this work, the purpose was to obtain samples with only anatase phase (confirmed by XRD results, as shown in Fig. 7.2).

However, as known by the literature, if rutile and anatase are in strict contact, a synergistic effect may emerge. The electrons produced into rutile are promoted to anatase covalent band and this phenomenon reduces the recombination rate into the rutile phase [41–43]. In fact, the charge separation process can be achieved thanks

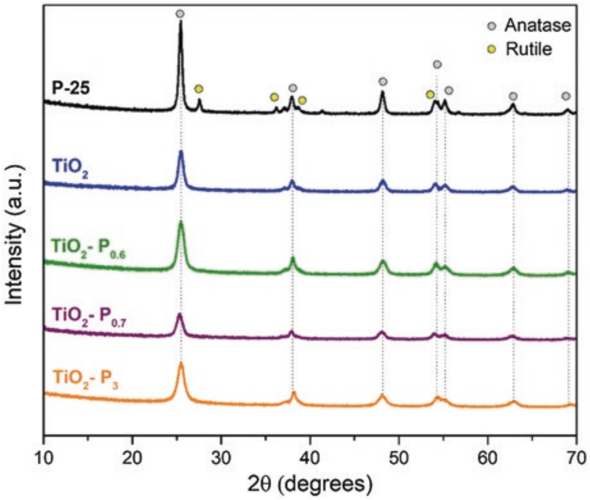

Fig. 7.2 XRD patterns of the synthesized samples along with commercial P-25 (by Degussa)

to this electron transfer to the rutile/anatase interface that is at lower energy state. The recombination phenomena decrease and electrons can easily move to TiO_2 conduction band [44]. As a whole, the presence of both anatase and rutile is beneficial in terms of photocatalytic activity due to the following issues [40]:

1. With the presence of both rutile and anatase phases, it is possible to extend the photocatalytic activity of titania at higher wavelength.
2. The charge separation from rutile to anatase is stabilized by the electron transfer and avoids the recombination phenomena of electron/hole pairs.
3. Rutile particles are characterized by smaller crystallite size, compared to anatase ones. This characteristic enhances the charge transfer because there are preferential points at the rutile/anatase interface (originated by the smaller rutile crystallites in close contact with the anatase phase) in which the photocatalytic phenomenon occurs.

7.3.2 FESEM and EDX Analysis

In Fig. 7.3 are reported the FESEM images for the prepared samples. As a whole, it appears that the prepared photocatalysts exhibit smaller particle sizes compared to the commercial material P-25.

To better investigate the particle sizes, the average diameters for each sample were analyzed by the ImageJ software [45]. The particle size distributions are reported in Fig. 7.4. The average diameter of the particles for the prepared samples

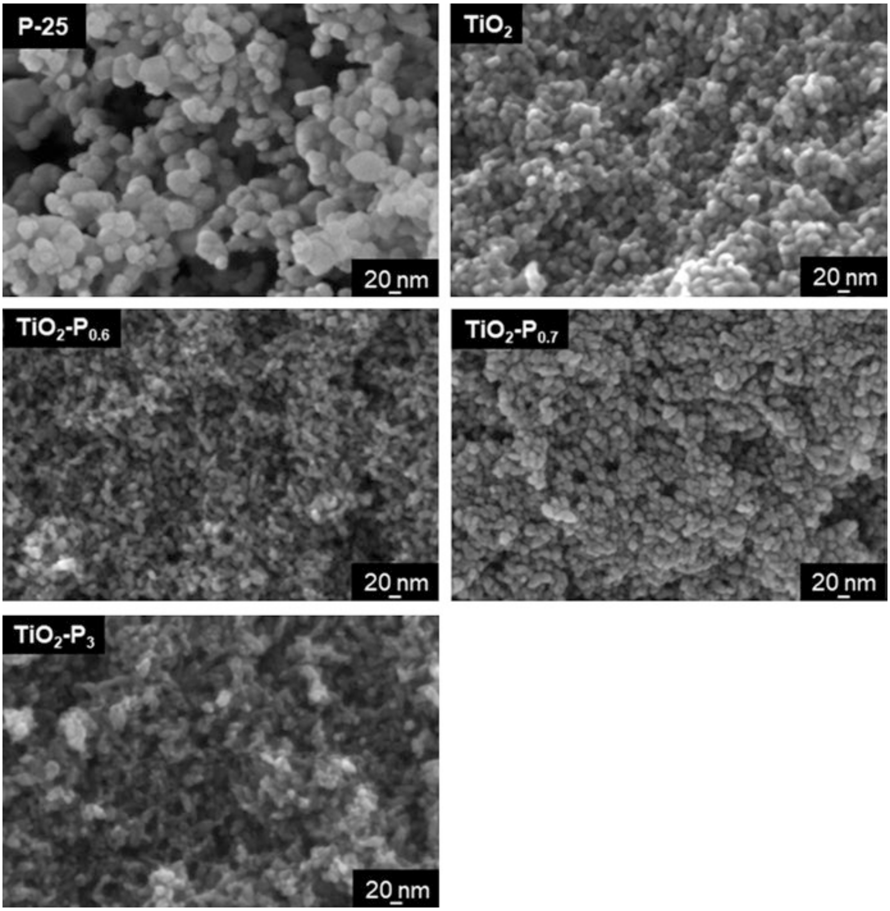

Fig. 7.3 FESEM images of the prepared samples along with the commercial P-25 (by Degussa)

is lower than 15 nm. In particular, the TiO_2-$P_{0.6}$ sample exhibits the lowest average particle diameter (about 9 nm) among the prepared photocatalysts. Moreover, these results are in agreement with the crystallite size: the higher the P-content, the smaller the crystallite, and the particle sizes.

The EDX analysis was performed over three different areas, in order to evaluate the P-content into doped-titania samples. The results are reported in Table 7.2. For all the samples, the average phosphorus content is close to the theoretical amount used during the synthesis procedure.

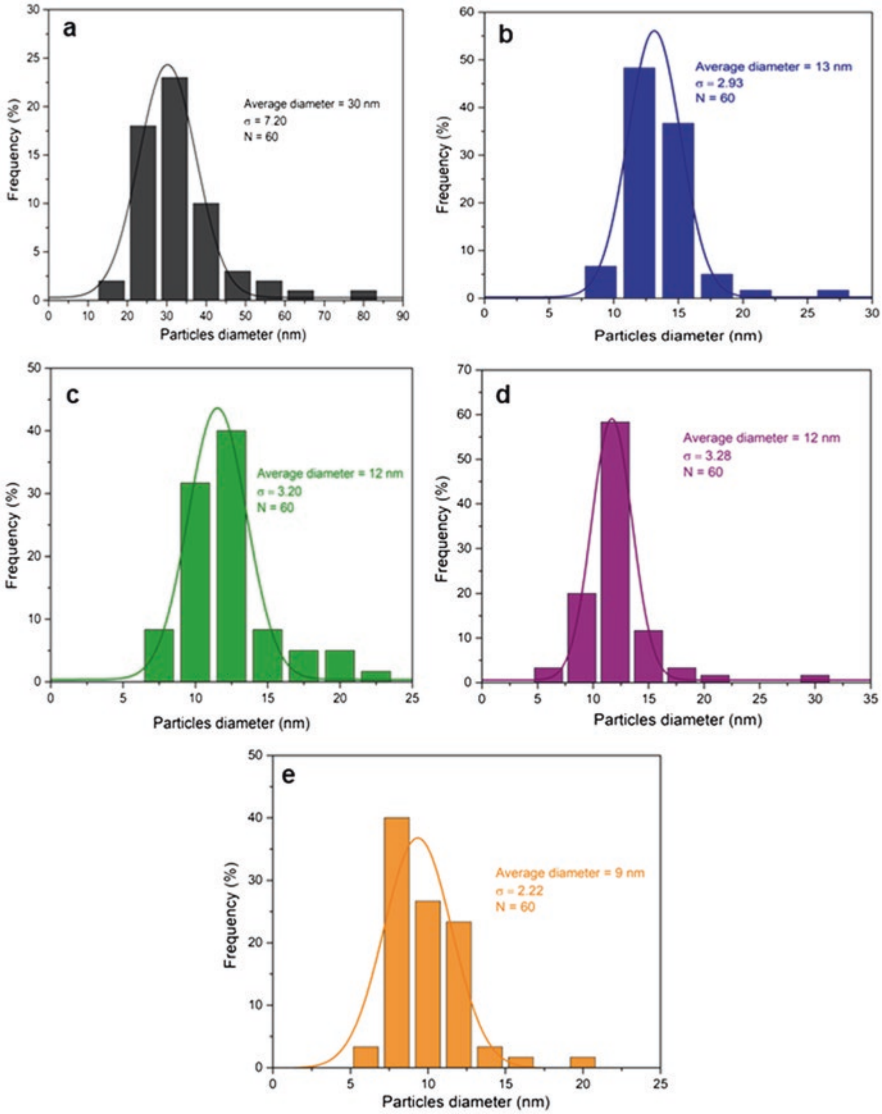

Fig. 7.4 Particles distribution analysis over (**a**) P-25, (**b**) TiO_2, (**c**) TiO_2-$P_{0.6}$, (**d**) TiO_2-$P_{0.7}$, and (**e**) TiO_2-P_3

7.3.3 XPS Analysis

Table 7.3 reports the XPS analysis of the prepared samples, as derived from the deconvolution peaks. As a whole, the synthesized catalysts have similar Ti and O contents (Ti/O ~ 1/3). This result is lower than the theoretical value of TiO_2 that is

Table 7.2 EDX analysis over the doped-titania samples investigated over three different areas

Elements	TiO_2-$P_{0.6}$	TiO_2-$P_{0.7}$	TiO_2-P_3
Ti	35.87	31.10	30.65
O	63.55	68.28	66.39
P	0.58	0.62	2.96
Tot.	100	100	100

Table 7.3 Elemental composition over the prepared samples derived from XPS analysis.

Catalysts	Ti (at.%)	O (at.%)	P (at.%)
TiO_2	26.8	73.2	–
TiO_2-$P_{0.6}$	26.9	71.6	1.5
TiO_2-$P_{0.7}$	27.0	71.6	1.4
TiO_2-P_3	22.7	73.2	4.1

about 1/2. As previously evidenced by the EDX analysis (*see* Table 7.2*,* Sect. 7.3.2), the bulk compositions of the doped samples exhibit the Ti-to-O ratio near to the theoretical value (1/2). On the other hand, according to the XPS analysis it appears that such materials present the Ti-to-O ratio near to 1/3.

These findings confirm the doped samples have higher amount of oxygen species on the surface rather than in the bulk.

The deconvoluted Ti 2*p* spectra are reported in Fig. 7.5. These spectra are characterized by a $2p_{3/2}$ spin-orbit peak (average binding energy (B.E.) = 458.8 eV) and a low-intensity peak in the $2p_{1/2}$ region. In particular, in the $2p_{3/2}$ region, two peaks appear: a signal at about 459 eV referred to Ti^{4+} and another component at about 457 eV assigned to Ti^{3+} [46]. The Ti^{4+} and Ti^{3+} abundancy was evaluated by the deconvolution of $2p_{3/2}$ region and the values (at.%) are reported in Table 7.4. The Ti^{3+}-to-Ti^{4+} ratio increases along with the P-content. Thus, the O-Ti-O bonding exhibits a weakening generated by the cation substitution into the titania framework.

The O 1*s* spectra are reported in Fig. 7.6. All the samples exhibit two characteristics peaks. One signal at lower B.E. (530 eV) related to bonded oxygens into the titania structure (Ti-O). Another one to higher B.E. (532–530 eV) associated to surface hydroxyl groups (O-H) [47–49]. For doped catalysts, an additional peak was observed at about 533 eV, herein labeled as “no lattice oxygen” (NLO*). According to the literature, this additional peak can be attributed to chemisorbed oxygen species on the catalysts surface [50, 51]. This NLO* peak is a characteristic only of the doped samples, since they are the samples with smaller crystallite sizes and with the higher probability to have more unsaturation on the catalyst’s surfaces (*see* Sect. 7.3.1). These surface defects are responsible of the hydroxyl groups chemisorption [36].

Table 7.5 summarizes the relative abundancy of oxygen species evaluated by the deconvolution of O 1*s* XP spectra. As previously noticed by the O 1*s* spectra, only the doped samples exhibit the NLO* oxygen species. The presence of such species along with OH groups can promote the VOC abatement due to the formation of OH radicals, which play a key role during the VOC oxidation [52].

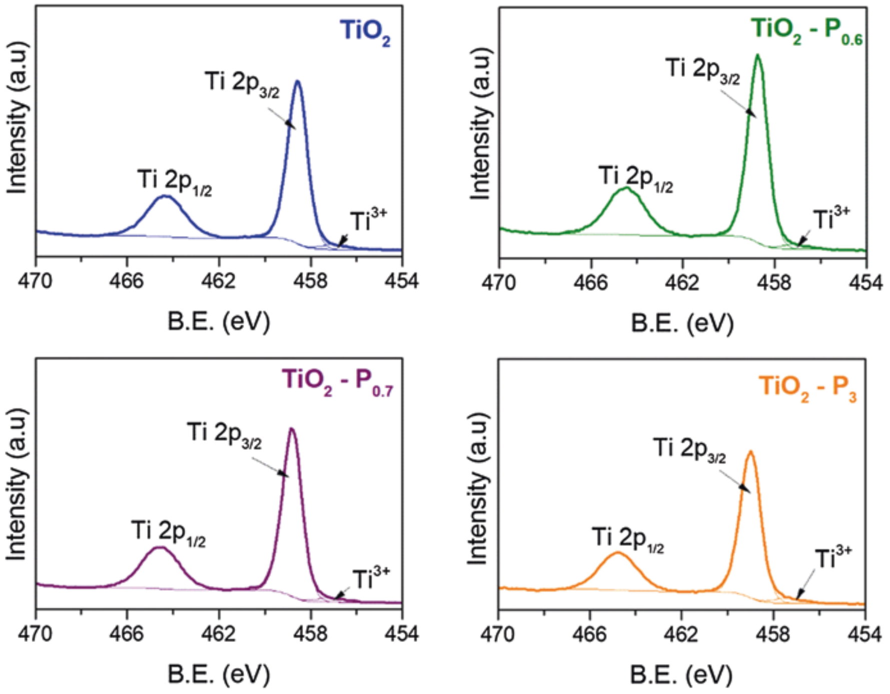

Fig. 7.5 Ti 2*p* X-ray photoelectron spectra of the samples

Table 7.4 Ti^{4+} and Ti^{3+} species observed on the catalyst surfaces evaluated by the deconvolution of Ti 2*p* XP spectra

	Ti 2*p*				
Catalysts	Ti^{4+} (at.%)	Position (B.E.)	Ti^{3+} (at.%)	Position (B.E.)	Ti^{3+}/Ti^{4+}
TiO$_2$	97.4	458.6	2.6	457.0	2.7
TiO$_2$-P$_{0.6}$	97.9	458.7	2.1	457.2	2.1
TiO$_2$-P$_{0.7}$	97.8	458.8	2.2	457.2	2.2
TiO$_2$-P$_3$	98.1	458.6	3.0	457.4	3.1

In Fig. 7.7 are reported the XP spectra for the P 2*p* core level to confirm the presence of P species on the catalyst surfaces. The position of the peaks occurs at about 134 eV corresponding to the P^{5+} species [46].

7.3.4 (DR)UV-Vis Spectroscopic Analysis

The (DR)UV-Vis spectra recorded for the synthesized catalysts are reported in Fig. 7.8. In particular, it appears that the absorption in the range 200–350 nm increases as a function of the P-content (Fig. 7.8 section a, TiO$_2$-P$_3$ is the sample that absorbs higher amount of light source in this range). The evaluation of the Band

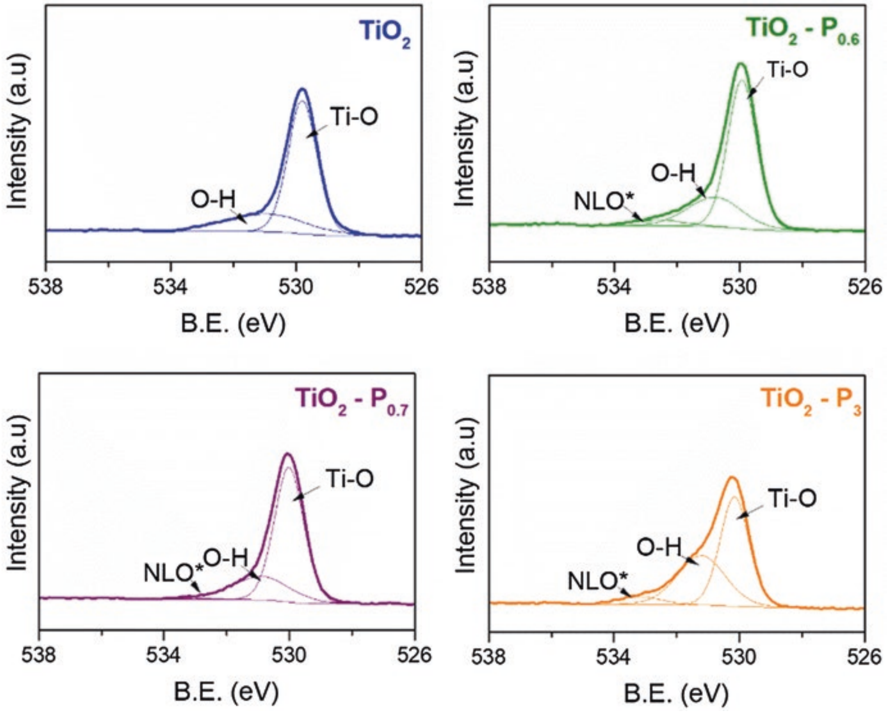

Fig. 7.6 O 1*s* X-ray photoelectron spectra of the samples

Table 7.5 Oxygen species on the catalyst surfaces as evaluated by the deconvolution of O 1*s* XP spectra

	O 1*s*					
Catalysts	Ti-O (at.%)	Position (B.E.)	O-H (at.%)	Position (B.E.)	NLO* (%)	Position (B.E.)
TiO_2	73.3	529.8	26.7	530.9	–	–
TiO_2-$P_{0.6}$	69.2	529.9	26.1	530.8	4.7	532.6
TiO_2-$P_{0.7}$	74.0	530.0	25.0	530.9	1.0	533.1
TiO_2-P_3	54.0	530.2	40.5	530.2	5.5	533.1

Gap energy was elaborated via the Tauc's plot (Fig. 7.8 sections b, c). The Band Gap Energies are reported in Table 7.6. Approximately, all the samples exhibit similar Band Gap Energies, corresponding to about 3.2 eV. During the photocatalytic phenomenon, this energy is required to promote the electrons from the valence band to the conduction band. In the present case, the catalyst with the lowest Band Gap Energy is the TiO_2-$P_{0.7}$ (3.13 eV). On the other hand, the highest Band Gap Energy can be observed for the TiO_2-P_3 sample (3.19 eV), along with TiO_2-$P_{0.6}$ (3.18 eV), thus suggesting higher absorption in the UV range [53].

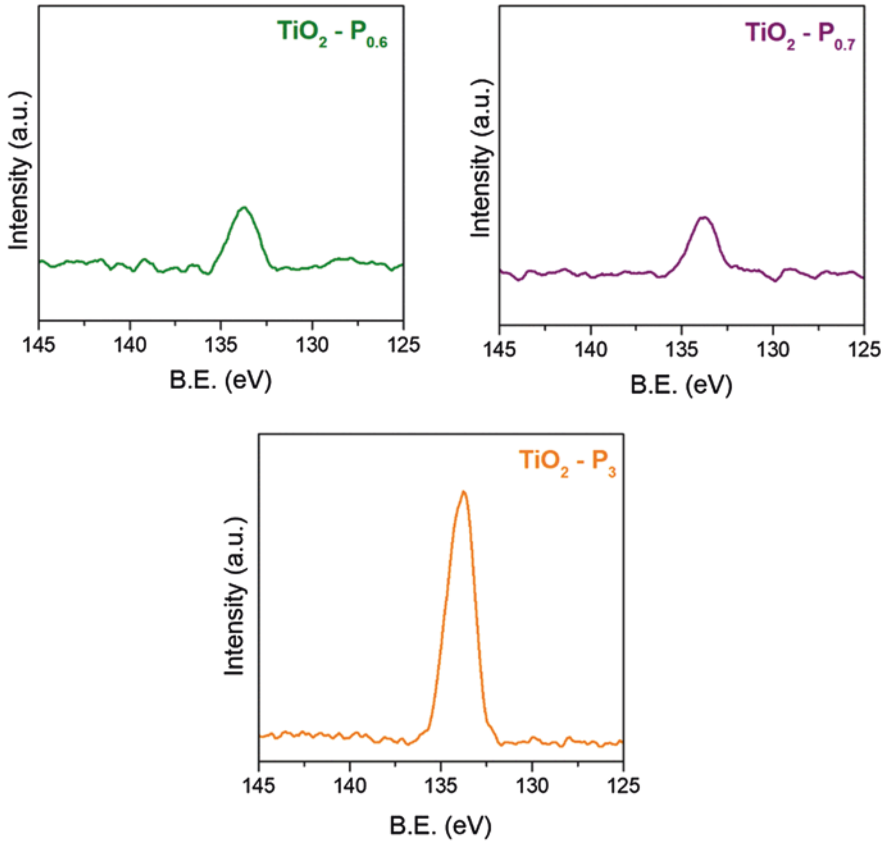

Fig. 7.7 P 2*p* X-ray photoelectron spectra of the doped samples

7.3.5 Catalytic Activity

The photocatalytic tests for the total oxidation of ethylene are reported in Fig. 7.9.

The ethylene conversion was studied for a TOS of 160 min. As a whole, the TiO_2 sample exhibited lower ethylene conversion compared to P-containing samples. In fact, as evidenced by our previous work [54] and other research studies [30, 55–61], the presence of phosphorus inside TiO_2 structure can enhance the photocatalytic activity as promoter element. This effect can be due to the possible modification of the crystalline and electronic structure of TiO_2 and then to the enhancedphotoabsorption mechanism (*see* Sect. 7.1*)*.

Noteworthy, all the photocatalysts are more reactive under the UVA source rather than with the UVB range, although the lower intensity (namely, 8 and 12 W m^{-2}, respectively). This finding confirms that P-containing titania samples can be effective at higher wavelengths, in agreement with the literature [30, 55–61].

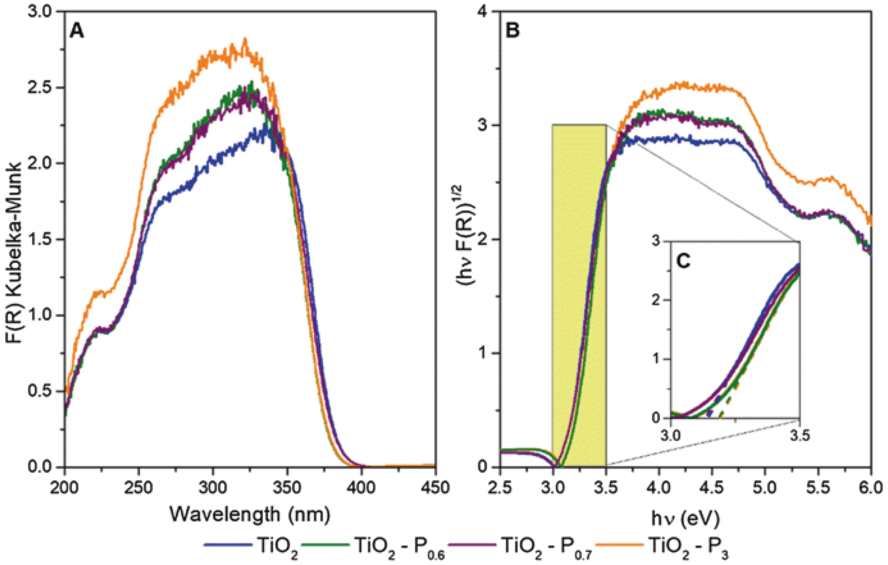

Fig. 7.8 (DR)UV-Vis spectra of the studied sample: (**a**) Kubelka-Munk plot, (**b**) Tauc's plot, and (**c**) Magnification of Tauc's plot

Table 7.6 Band Gap Energies (eV) evaluated over the studied catalysts.

Catalyst	Band gap energy (eV)
TiO_2	3.14
TiO_2-$P_{0.6}$	3.18
TiO_2-$P_{0.7}$	3.13
TiO_2-P_3	3.19

In order to better clarify the photocatalytic activity, the TOF was analyzed over the samples at two different reaction times (40 and 160 min). The results are reported in Fig. 7.10. The TOF values evaluated at 40 and 160 min show a positive trend as a function of the P-contents for the samples tested under UVB. The higher the P-content, the higher the reactivity. Thus, the best performing catalyst is the TiO_2-P_3, in agreement with the (DR)UV-Vis spectra. A similar trend, although less evident, can be observed for the samples tested under UVA. Nevertheless, in the latter case, it appears that samples with higher P-contents exhibited a lower reactivity at longer TOS, likely due to partial surface coverage by the presence of carbon-like molecules. Conversely, the optimum is reached with the TiO_2-$P_{0.6}$ sample (21.3 μmol h^{-1} g^{-1}).

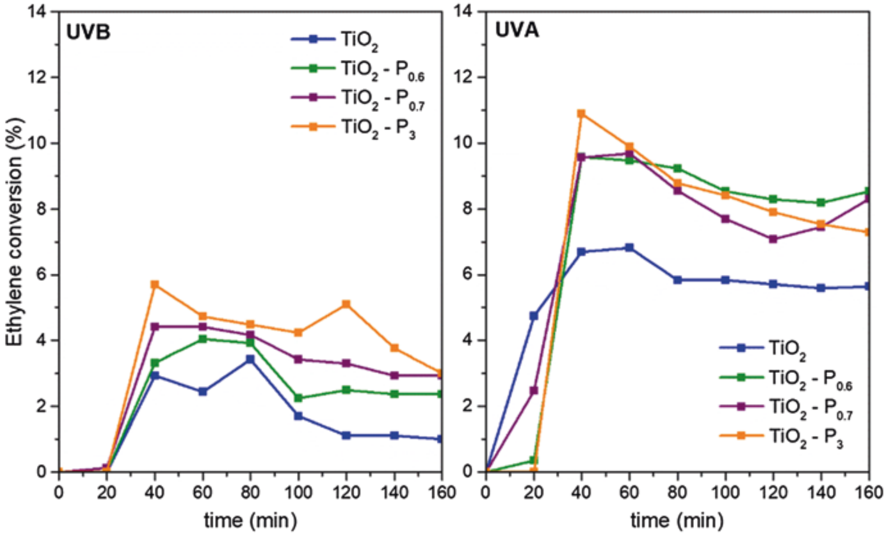

Fig. 7.9 Photocatalytic tests over the synthesized samples under two different sources: UVB and UVA

7.4 Conclusions

In this study, a set of phosphorous-doped titania were synthesized, at different P-contents, namely 0.6, 0.7, and 3 at.%. Pure TiO_2 was prepared for comparison purposes. All the synthesized samples had the presence of pure anatase and it was found that the incorporation of phosphorus into the solids renders the crystallite smaller.

Similarly, better textural properties were obtained with P-containing samples compared to pure TiO_2. UV-Vis spectroscopy confirmed a more intense absorption in the UV range for the P-containing samples. Catalytic results have shown a positive trend as a function of the P-contents for the samples tested under UVB. The higher the P-content, the higher the reactivity. A similar trend, although less evident, was for the samples tested under UVA. Nevertheless, in the latter case, it appears that samples with higher P-contents exhibited lower reactivity at longer TOS, likely due to the surface deposition of carbon-like molecules.

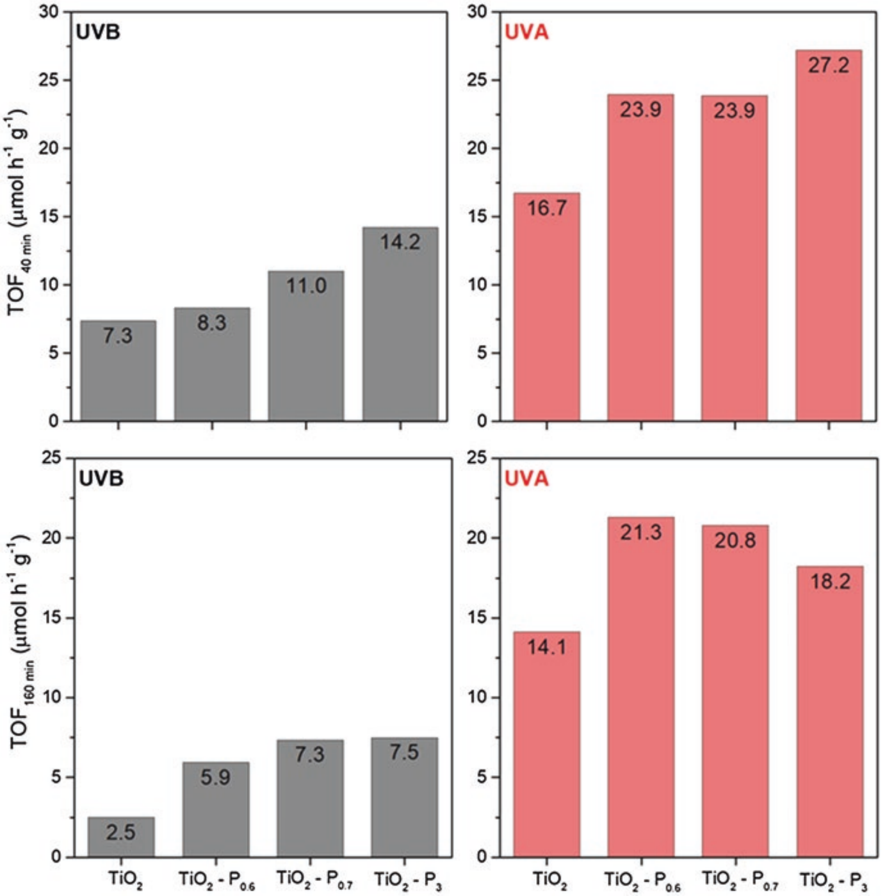

Fig. 7.10 TOF evaluated at 40 min (above) and 160 min (below) under different sources

References

1. Council of the European Parliament, Council Directive 1999/13/EC of 11 March 1999 on the limitation of emissions of volatile organic compounds due to the use of organic solvents in certain activities and installations, Off. J. Eur. Comm. L85/1–L85/22 (1999)
2. W.B. Li, J.X. Wang, H. Gong, Catalytic combustion of VOCs on non-noble metal catalysts. Catal. Today **148**, 81–87 (2010)
3. S. Ojala, S. Pitkäaho, T. Laitinen, N. NiskalaKoivikko, R. Brahmi, J. Gaálová, L. Matejova, A. Kucherov, S. Päivärinta, C. Hirschmann, T. Nevanperä, M. Riihimäki, M. Pirilä, R.L. Keiski, Catalysis in VOC abatement. Top. Catal. **54**, 1224–1256 (2011)
4. E. Olsen, F. Nielsen, Predicting vapour pressures of organic compounds from their chemical structure for classification according to the VOC-directive and risk assessment in general. Molecules **6**, 370–389 (2001)
5. M.S. Kamla, S.A. Razzak, M.M. Hossain, Catalytic oxidation of volatile organic compounds (VOCs)—a review. Atmos. Environ. **140**, 117–134 (2016)

6. P. Doggali, Y. Teraoka, P. Mungse, I.K. Shah, S. Rayalu, N. Labhsetwar, Combustion of volatile organic compounds over Cu-Mn based mixed oxide type catalysts supported on mesoporous Al_2O_3, TiO_2 and ZrO_2. J. Mol. Catal. A Chem. **358**, 23–30 (2012)
7. J. Carpentier, J.F. Lamonier, S. Siffert, E.A. Zhilinskaya, A. Aboukas, Characterisation of Mg/Al hydrotalcite with interlayer palladium complex for catalytic oxidation of toluene. Appl. Catal. A Gen. **234**, 91–101 (2002)
8. F.I. Khan, A.K. Ghoshal, Removal of volatile organic compounds from polluted air. J. Loss Prev. Process Ind. **13**, 527–545 (2000)
9. G.S.P. Soylu, Z. Özçelik, I. Boz, Total oxidation of toluene over metal oxides supported on a natural clinoptilolite-type zeolite. Chem. Eng. J. **162**, 380–387 (2010)
10. B. Ozturk, D. Yilmaz, Absorptive removal of volatile organic compounds from flue gas streams. Process Saf. Environ. Prot. **84**, 391–398 (2006)
11. M. Amann, M. Lutz, The revision of the air quality legislation in the European Union related to ground-level ozone. J. Hazard. Mater. **78**, 41–62 (2000)
12. P. Lakshmanan, L. Delannoy, V. Richard, C. Méthivier, C. Potvin, C. Louis, Total oxidation of propene over Au/xCeO_2-Al_2O_3 catalysts: influence of the CeO_2 loading and the activation treatment. Appl. Catal. B Environ. **96**, 117–125 (2010)
13. M.J. Molina, F.S. Rowland, *Stratospheric Sink for Chlorofluoromethanes: Chlorine Atom-Catalysed Destruction of Ozone* (Academic Press, New York, 1973)
14. J. Peng, S. Wang, Performance and characterization of supported metal catalysts for complete oxidation of formaldehyde at low temperatures. Appl. Catal. B Environ. **73**, 282–291 (2007)
15. B.J. Finlayson-Pitts, J.N. Pitts, Tropospheric air pollution: ozone, airborne toxics, polycyclic aromatic hydrocarbons, and particles. Science **276**, 1045–1052 (1997)
16. H. Rodhe, A comparison of the contribution of various gases to the greenhouse effect. Science **248**, 1217–1219 (1990)
17. M. Drobek, A. Figoli, S. Santoro, N. Navascués, J. Motuzas, S. Simone, C. Algieri, N. Gaeta, L. Querze, A. Trotta, G. Barbieri, R. Mallada, A. Julbe, E. Drioli, PVDF-MFI mixed matrix membranes as VOCs adsorbers. Micropor. Mesopor. Mater. **207**, 126–133 (2015)
18. S. Scirè, L.F. Liotta, Supported gold catalysts for the total oxidation of volatile organic compounds. Appl. Catal. B Environ. **125**, 222–246 (2012)
19. R. Koppmann, *Volatile Organic Compounds in the Atmosphere* (Wiley Online Library, Hoboken, 2007)
20. EPA, United Stated Environmental Protection Agency, Indoor Air Quality (IAQ), https://www.epa.gov/indoor-air-quality-iaq/introduction-indoor-air-quality
21. M. Magureanu, N.B. Mandache, P. Eloy, E.M. Gaigneaux, V.I. Parvulescu, Plasma-assisted catalysis for volatile organic compounds abatement. Appl. Catal. B Environ. **61**, 12–20 (2005)
22. A.H. Wani, R.M.R. Branion, A.K. Lau, Biofiltration: a promising and cost-effective control technology for odors, VOCs and air toxics. J. Environ. Sci. Heal. Part A Environ. Sci. Eng. Toxicol. **32**, 2027–2055 (1997)
23. M. Hussain, N. Russo, G. Saracco, Photocatalytic abatement of VOCs by novel optimized TiO_2 nanoparticles. Chem. Eng. J. **166**, 138–149 (2011)
24. M.A. Fox, M.T. Dulay, Heterogeneous photocatalysis. Chem. Rev. **93**, 341–357 (2002)
25. M.R. Hoffmann, S.T. Martin, W. Choi, D.W. Bahnemann, Environmental applications of semiconductor photocatalysis. Chem. Rev. **95**, 69–96 (1995)
26. A. Hagfeldt, M. Grätzel, Light-induced redox reactions in nanocrystalline systems. Chem. Rev. **95**, 49–68 (1995)
27. X. Chen, S.S. Mao, Titanium dioxide nanomaterials: synthesis, properties, modifications and applications. Chem. Rev. **107**, 2891–2959 (2007)
28. M.A. Henderson, A surface science perspective on TiO_2 photocatalysis. Surf. Sci. Rep. **66**, 185–297 (2011)
29. Z. Zhang, S. Brown, J.B.M. Goodall, X. Weng, K. Thompson, K. Gong, S. Kellici, R.J.H. Clark, J.R.G. Evans, J.A. Darr, Direct continuous hydrothermal synthesis of high surface area nanosized titania. J. Alloys Compd. **476**, 451–456 (2009)

30. P. Zhang, Y. Yu, E. Wang, J. Wang, J. Yao, Y. Cao, Structure of nitrogen and zirconium co-doped titania with enhanced visible-light photocatalytic activity. ACS Appl. Mater. Interfaces **6**, 4622–4629 (2014)
31. M.D. Hernández-Alonso, J.M. Coronado, B. Bachiller-Baeza, M. Fernández-García, J. Soria, Influence of structural and surface characteristics of Ti 1-xZrxO2 nanoparticles on the photocatalytic degradation of methylcyclohexane in the gas phase. Chem. Mater. **19**, 4283–4291 (2007)
32. W. Zhao, W. Ma, C. Chen, J. Zhao, Z. Shuai, Efficient degradation of toxic organic pollutants with Ni2O 3/TiO2-xBx under visible irradiation. J. Am. Chem. Soc. **126**, 4782–4783 (2004)
33. Y. Cong, J. Zhang, F. Chen, M. Anpo, D. He, Preparation, photocatalytic activity, and mechanism of nano-TiO2 Co-doped with nitrogen and iron (III). J. Phys. Chem. C **111**, 10618–10623 (2007)
34. S. Shamaila, A.K.L. Sajjad, F. Chen, J.L. Zhang, Synthesis and characterization of mesoporous-TiO_2 with enhanced photocatalytic activity for the degradation of chloro-phenol. Mater. Res. Bull. **45**, 1375–1382 (2010)
35. M. Piumetti, F.S. Freyria, M. Armandi, F. Geobaldo, E. Garrone, B. Bonelli, Fe- and V-doped mesoporous titania prepared by direct synthesis: characterization and role in the oxidation of AO7 by H_2O_2 in the dark. Catal. Today **227**, 71–79 (2014)
36. N. Musselwhite, G.A. Somorjai, Investigations of structure sensitivity in heterogeneous catalysis: from single crystals to monodisperse nanoparticles. Top. Catal. **56**, 1277–1283 (2013)
37. R.A. Van Santen, Complementary structure sensitive and insensitive catalytic relationships. Acc. Chem. Res. **42**, 57–66 (2009)
38. G. Li, L. Li, J. Boerio-Goates, B.F. Woodfield, High purity anatase TiO_2 nanocrystals: near room-temperature synthesis, grain growth kinetics, and surface hydration chemistry. J. Am. Chem. Soc. **127**, 8659–8666 (2005)
39. B. Ohtani, O.O. Prieto-Mahaney, D. Li, R. Abe, What is Degussa (Evonic) P25? Crystalline composition analysis, reconstruction from isolated pure particles and photocatalytic activity test. J. Photochem. Photobiol. A Chem. **216**, 179–182 (2010)
40. L.P. Childs, D.F. Ollis, Is photocatalysis catalytic? J. Catal. **66**, 383–390 (1980)
41. G. Li, C.P. Richter, R.L. Milot, L. Cai, C.A. Schmuttenmaer, R.H. Crabtree, G.W. Brudvig, V.S. Batista, Synergistic effect between anatase and rutile TiO2 nanoparticles in dye-sensitized solar cells. J. Chem. Soc. Dalton Trans. **45**, 10078–10085 (2009)
42. J. Zhang, P. Zhou, J. Liu, J. Yu, New understanding of the difference of photocatalytic activity among anatase, rutile and brookite TiO_2. Phys. Chem. Chem. Phys. **16**, 20382–20386 (2014)
43. D.S. Bhatkhande, V.G. Pangarkar, A.A. Beenackers, Photocatalytic degradation for environmental applications—a review. J. Chem. Technol. Biotechnol. **77**, 102–116 (2002)
44. R.R. Guimaraes, A.L.A. Parussulo, K. Araki, Impact of nanoparticles preparation method on the synergic effect in anatase/rutile mixtures. Electrochim. Acta **222**, 1378–1386 (2016)
45. M.D. Abràmoff, P.J. Magalhães, S.J. Ram, Image processing with imageJ. Biophoton. Int. **11**, 36–41 (2004)
46. J.F. Moulder, W.F. Stickle, P.E. Sobol, K.D. Bomben, *Handbook of Photoelectron Spectroscopy* (Perkin-Elmer Corporation, Eden Prairie, 1992)
47. M.M. Kumar, S. Badrinarayanan, M. Sastry, Nanocrystalline TiO_2 studied by optical, FTIR and X-ray photoelectron spectroscopy: correlation to presence of surface states. Thin Solid Films **358**, 122–130 (2000)
48. Y.D. Hou, X.Z. Fu, X.X. Wang, X.C. Wang, X.F. Chen, Z.X. Ding, L. Wu, N-doped SiO_2/TiO_2 mesoporous nanoparticles with enhanced photocatalytic activity under visible-light irradiation. Chemosphere **72**, 414–421 (2008)
49. S. Begin, G. Bertrand, F. Toma, O. Barres, C. Coddet, C. Meunier, D. Klein, Microstructure and environmental functionalities of TiO_2-supported photocatalysts obtained by suspension plasma spraying. Appl. Catal. B Environ. **68**, 74–84 (2006)
50. B. Bharti, S. Kumar, H.N. Lee, R. Kumar, Formation of oxygen vacancies and Ti^{3+} state in TiO_2 thin film and enhanced optical properties by air plasma treatment. Sci. Rep. **6**, 1–12 (2016)

51. S. Wang, L. Pan, J.J. Song, W. Mi, J.J. Zou, L. Wang, X. Zhang, Titanium-defected undoped anatase TiO2 with p-type conductivity, room-temperature ferromagnetism, and remarkable photocatalytic performance. J. Am. Chem. Soc. **137**, 2975–2983 (2015)
52. S. Futamura, H. Einaga, H. Kabashima, L.Y. Hwan, Synergistic effect of silent discharge plasma and catalysts on benzene decomposition. Catal. Today **89**, 89–95 (2004)
53. J.C. Yu, L. Zhang, Z. Zheng, J. Zhao, Synthesis and characterization of phosphated mesoporous titanium dioxide with high photocatalytic activity. Chem. Mater. **15**, 2280–2286 (2003)
54. M. Dosa, M. Piumetti, S. Bensaid, T. Andana, C. Galletti, D. Fino, N. Russo, Photocatalytic abatement of volatile organic compounds by TiO2 nanoparticles doped with either phosphorous or zirconium. Materials **12**, 2121 (2019)
55. E. Wang, T. He, L. Zhao, Y. Chen, Y. Cao, Improved visible light photocatalytic activity of titania doped with tin and nitrogen. J. Mater. Chem. **21**, 144–150 (2011)
56. F. Freyria, M. Compagnoni, N. Ditaranto, I. Rossetti, M. Piumetti, G. Ramis, B. Bonelli, Pure and Fe-doped mesoporous titania catalyse the oxidation of acid orange 7 by H_2O_2 under different illumination conditions: Fe doping improves photocatalytic activity under simulated solar light. Catalysts **7**, 213 (2017)
57. L. Lin, W. Lin, J.L. Xie, Y.X. Zhu, B.Y. Zhao, Y.C. Xie, Photocatalytic properties of phosphor-doped titania nanoparticles. Appl. Catal. B Environ. **75**, 52–58 (2007)
58. S. Guo, S. Han, M. Haifeng, C. Zeng, Y. Sun, B. Chi, J. Pu, J. Li, Synthesis of phosphorus-doped titania with mesoporous structure and excellent photocatalytic activity. Mater. Res. Bull. **48**, 3032–3036 (2013)
59. J.C.-S. Wu, C.H. Chen, A visible-light response vanadium-doped titania nanocatalyst by sol-gel method. J. Photochem. Photobiol. A Chem. **163**, 509–515 (2004)
60. K. Wilke, H.D. Breuer, The influence of transition metal doping on the physical and photocatalytic properties of titania. J. Photochem. Photobiol. A Chem. **121**, 49–53 (1999)
61. J. Reszczyńska, T. Grzyb, J.W. Sobczak, W. Lisowski, M. Gazda, B. Ohtani, A. Zaleska, Visible light activity of rare earth metal doped (Er^{3+}, Yb^{3+} or Er^{3+}/Yb^{3+}) titania photocatalysts. Appl. Catal. B Environ. **163**, 40–49 (2015)